

Coherent steering of nonlinear chiral valley photons with a synthetic Au-WS₂ metasurface

Guangwei Hu^{1,9}, Xuanmiao Hong^{2,9}, Kai Wang^{1,9}, Jing Wu³, He-Xiu Xu^{1,8}, Wenchao Zhao², Weiwei Liu², Shuang Zhang⁴, Francisco Garcia-Vidal^{5,6}, Bing Wang², Peixiang Lu^{1,9} and Cheng-Wei Qiu^{1*}

Two-dimensional transition metal dichalcogenides (TMDCs) present extraordinary nonlinearities and direct bandgaps at the K and K' valleys. These valleys can be optically manipulated through, for example, plasmon-valley-exciton coupling with spin-dependent photoluminescence. However, the weak coherence between the pumping and emission makes exploring nonlinear valleytronic devices based on TMDCs challenging. Here, we show that a synthetic metasurface, which entangles the phase and spin of light, can simultaneously enhance and manipulate nonlinear valley-locked chiral emission in monolayer tungsten disulfide (WS₂) at room temperature. The second-harmonic valley photons, accessed and coherently pumped by light, with a spin-related geometric phase imparted by a gold (Au) metasurface, are separated and routed to predetermined directions in free space. In addition, the nonlinear photons with the same spin as the incident light are steered owing to the critical spin-valley-locked nonlinear selection rule of WS₂ in our designed metasurface. Our synthetic TMDC-metasurface interface may facilitate advanced room-temperature and free-space nonlinear, quantum and valleytronic nanodevices.

The optical properties of two-dimensional (2D) semiconductors are dominated by excitonic effects. In particular, TMDCs have a direct bandgap in the visible region at the energetically degenerate K and K' (−K) points of their hexagonal Brillouin zones, the so-called valleys. Inversion symmetry and strong spin-orbit interaction in TMDCs lead to spin-valley locking at K and K' valleys. TMDCs can therefore support two different types of energetically degenerate exciton, which are identical except that they have opposite Berry curvatures. Consequently, the two types of exciton exhibit distinct responses to light of different helicity depending on their valley pseudospin^{1–4}. To take advantage of this effect and build feasible valleytronic devices for optoelectronic applications, this valley degree of freedom must be accessed through the different responses to external stimuli such as electric, magnetic and optical fields^{4–7}. Various applications in optoelectronics and valleytronics have been realized using the spin-valley effect^{4,5,8–13}. However, the lifetime of the valley excited state is typically very short¹⁴, especially at room temperature, making it difficult to maintain the coherence of the valley and manipulate its index. Moreover, light-matter interaction in atomically thin TMDCs is very weak, and is even weaker in nonlinear conversion processes such as second-harmonic generation (SHG). This limitation hinders the possibility of nonlinear valleytronic devices based on 2D TMDCs, which are necessary for valley-multiplexed data transport^{15–19}. Therefore, it is important to establish viable approaches to the design of nanophotonic structures that, when combined with 2D TMDCs, could both boost the efficiency of nonlinear processes and exploit their valley index.

Optical metasurfaces^{20,21} with subwavelength meta-atoms have emerged as important flat-profile platforms in nanophotonics capable of manipulating light properties including phase, amplitude, spin, frequency and chirality. Optical metasurfaces enable applications such as metalenses^{22,23}, metaholograms²⁴, carpet cloaking²⁵ and many others^{26–29}. In particular, plasmonic metasurfaces in which a photonic spin-orbit interaction is devised can discriminate photon spins and apply a spin-related geometric phase to light. In this way, different spin components can be spatially separated, an effect known as the photonic spin-Hall effect^{30–35}. As a counterpart to free-space photonic spin-Hall metasurfaces, gratings with asymmetric corrugations or nanoholes have been used to launch unidirectional surface plasmon polaritons^{33,36,37}. When these surface plasmon polaritons evanescently interact with excitons in 2D TMDCs in the near field, the subsequent spin-dependent directional photoluminescence carries the valley information to where the exciton is primarily generated^{38,39}. However, the photoluminescence generation process makes the coherence of the pumping and excited fields so weak that valley-exciton emission is very difficult to manipulate for practical applications. This issue becomes more serious when simultaneous control of the valley index in the nonlinear regime and enhancement of the spin-Hall effects are required to occur in free space instead of in the near field.

Here, we theoretically propose and experimentally demonstrate a metasurface-assisted photonic pathway to boost the coherent spin-valley-dependent nonlinear optical process in monolayer TMDCs and to steer the nonlinear photons from different valleys in any desired direction in free space at room temperature. As shown

¹Department of Electrical and Computer Engineering, National University of Singapore, Singapore, Singapore. ²Wuhan National Laboratory for Optoelectronics and School of Physics, Huazhong University of Science and Technology, Wuhan, China. ³Institute of Materials Research and Engineering, A*STAR (Agency for Science, Technology and Research), Singapore, Singapore. ⁴School of Physics and Astronomy, University of Birmingham, Birmingham, UK. ⁵Departamento de Física Teórica de la Materia Condensada and Condensed Matter Physics Center (IFIMAC), Universidad Autónoma de Madrid, Madrid, Spain. ⁶Donostia International Physics Center (DIPC), Donostia/San Sebastian, Spain. ⁷Laboratory of Optical Information Technology, Wuhan Institute of Technology, Wuhan, China. ⁸Present address: Air and Missile Defense College, Air force Engineering University, Xi'an, China. ⁹These authors contributed equally: Guangwei Hu, Xuanmiao Hong. *e-mail: kale_wong@hust.edu.cn; lupeixiang@hust.edu.cn; chengwei.qiu@nus.edu.sg

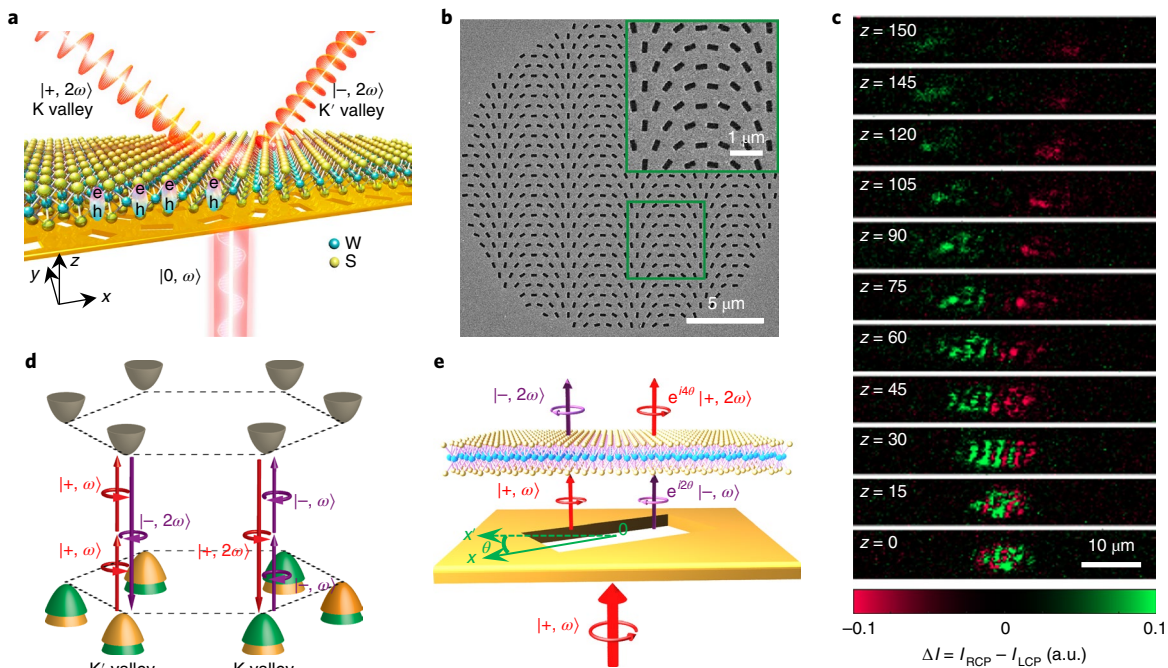


Fig. 1 | Concept, main result and principle of the synthetic Au-WS₂ metasurface. **a** Schematic of our synthetic Au-WS₂ metasurface. The single-layer WS₂ sits on top of a Au metasurface. Following the introduction of incident linearly polarized light ($|0, \omega\rangle$), where ω denotes the pumping frequency, the synthetic structure can yield large SHG from the valley band of the WS₂ and split opposite spin components of the second-harmonic valley photons ($|+, 2\omega\rangle$ and $|- , 2\omega\rangle$) into different directions. **b**, SEM image of the photonic spin-Hall metasurface. It is composed of rectangular nano-holes with different local rotation angles. **c**, The experimentally measured differential energy distribution (ΔI , the difference between the RCP intensity, I_{RCP} , and the LCP intensity, I_{LCP}) and evolution of the second-harmonic signal along the propagation direction (z , in μm), which is normalized by the maximum measured total intensity in the $z=0$ plane. **d**, Interband valley-exciton-locked SHG selection rule of hexagonal momentum space between the conduction band (grey) and valley band (green and yellow). **e**, Schematic of the physics principles of the valley-photon interface in our hybridized structures. θ denotes the rotation angle of a nano-hole with respect to the x axis.

in Fig. 1a, our synthetic Au-WS₂ metasurface contains two parts: the plasmonic Au metasurface (Fig. 1b) and the monolayer WS₂ on top of it. This metasurface is designed in such a way that the spin-valley-exciton-locked SHG occurs at the excitonic resonance of the K and K' valleys in monolayer WS₂^{6,12}. In addition, the plasmonic metasurface is able to enhance the nonlinear process responsible for SHG owing to large plasmonic field localization around the nano-holes. The Au metasurface imposes a chirality-dependent Pancharantnam-Berry phase gradient^{40–42}, which arises from the photonic spin-orbit interaction, to the fundamental-frequency light. This gradient pumps the coherent SHG process and, consequently, steers nonlinear chiral photons emitted from different valleys in different spatial directions (Fig. 1c).

Principle of steering nonlinear chiral valley photons

Here we present the theoretical foundation of our proposal for steering nonlinear chiral valley photons by means of a designed Au-TMDC metasurface. We first discuss the inherent nonlinear properties of monolayer WS₂. Owing to its topological properties of broken inversion symmetry and $D_{3h}(\bar{6}m2)$ symmetry in the SHG process, there is a complex interplay between the different momenta involved—the out-of-plane valley angular momentum, the excitonic angular momentum, the lattice angular momentum and the photon spin angular momentum—according to the fundamental angular momentum conservation law⁶. This leads to a nonlinear selection rule^{6,12,15}, whereby two fundamental-frequency photons of a given helicity are converted, with a second-harmonic exciton of opposite helicity generated (see Fig. 1d). This rule can be understood mathematically by looking at the non-vanishing components

of the second-harmonic susceptibility tensor of the D_{3h} point group, $\chi_{aaa}^{(2)} = -\chi_{qbb}^{(2)} = -\chi_{bba}^{(2)} = -\chi_{bab}^{(2)}$, where a and b are the principal directions of the monolayer, along the armchair and zigzag directions, respectively (see Supplementary Section 4 for more details). This selection rule is completely different from the incoherent photoluminescence process, in which the spin of the pumping and generated photons for one specific valley must be the same^{45,43}. Therefore, although originating from the lattice symmetry of the WS₂ monolayer, the valley-contrasting physics associated with the nonlinear process of SHG is non-trivial.

SHG is a coherent phenomenon, and thus provides the possibility of controlling and tuning second-harmonic photons by manipulating the fundamental-frequency photons that trigger the nonlinear process. This is exactly what our designed Au metasurface does. As shown in Fig. 1b, the Au metasurface is composed of an array of rectangular nano-holes with spatially varied rotation angle θ . Each nano-hole forms an individual resonator (see Supplementary Fig. 3d,e) and can be treated as a birefringent wave plate²⁹ with an associated Jones matrix

$$J(\theta) = T(-\theta) \begin{bmatrix} t_x & 0 \\ 0 & t_y \end{bmatrix} T(\theta)$$

where t_x and t_y denote the transmission coefficients along the two orthogonal principal axes and $T(\cdot)$ is the rotation matrix. The Jones matrix connects the output field (\mathbf{E}^{out}) and incident field (\mathbf{E}^{inc}) via $\mathbf{E}^{\text{out}} = J(\theta)\mathbf{E}^{\text{inc}}$. In this way, a spin-dependent geometric phase can be imprinted into the output fundamental-frequency field, which

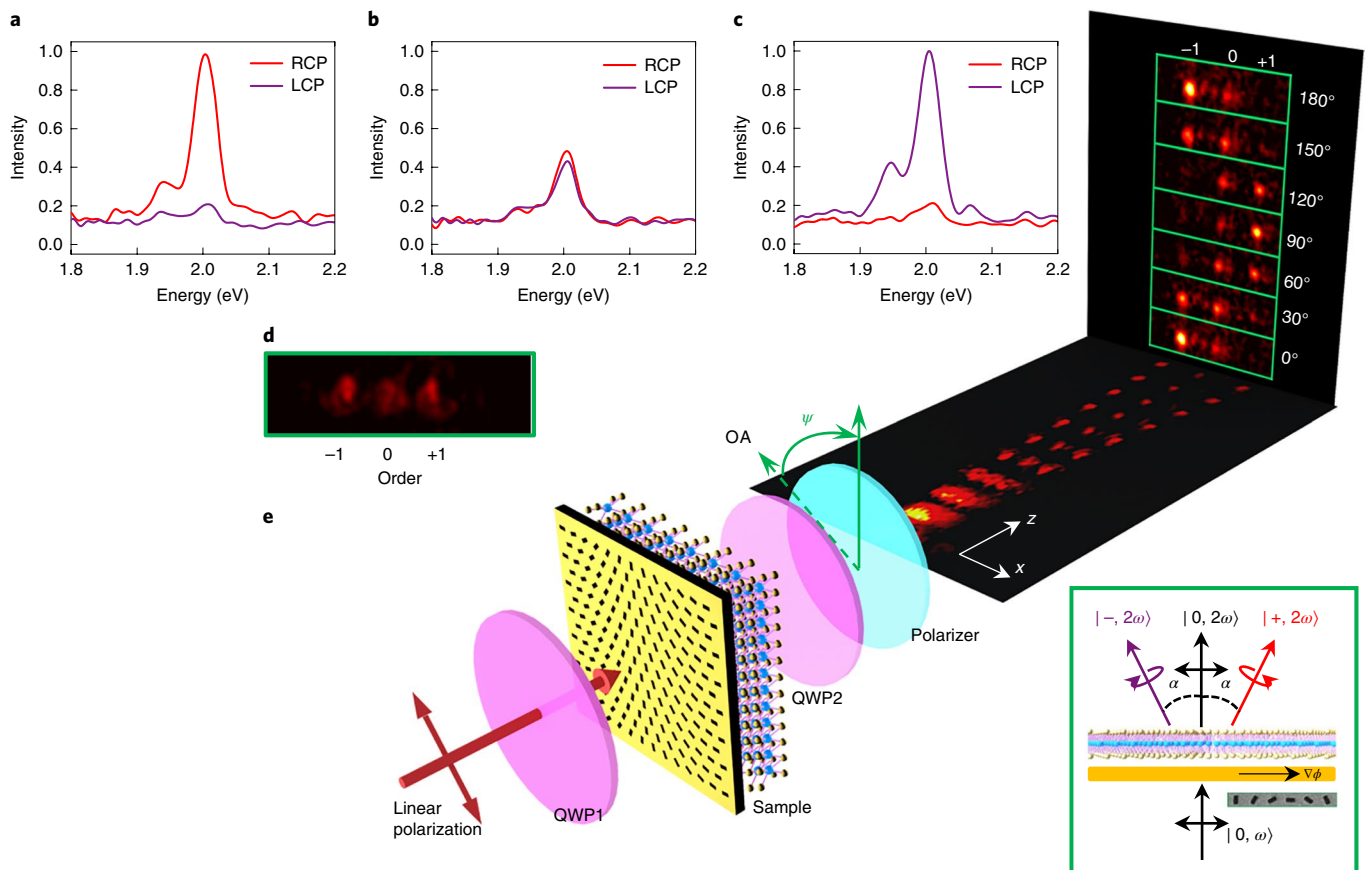


Fig. 2 | The optical set-up and experimental results under linearly polarized pumping. **a–c**, The experimentally measured intensity of the two chiral components in the 1st (**a**), 0th (**b**) and –1st orders (**c**), normalized by the maximum intensity of one spin component in that order. **d**, The field distribution at $z = 120 \mu\text{m}$, with three obvious orders. It is measured without QWP2 and the polarizer. **e**, Schematic of the experimental optical set-up. The incident linearly polarized beam has a wavelength of $1,240 \text{ nm}$. QWP1 can change the incident polarization to circularly polarized. QWP2 and the linear polarizer are used to test the chirality of the emitted second-harmonic photons. The horizontal image is the experimental result from the evolution of the light splitting into three orders. The vertical images are the field distributions obtained by rotating the linear polarizer, changing its optical axis (OA) by ψ . Inset: a schematic of the function of the Au-WS₂ metasurface. The inset SEM image shows one period of the nanohole array in the range of Λ .

further excites the SHG of monolayer WS₂ on top of the metasurface (see Fig. 1e). For example, incident right circularly polarized (RCP) light ($|+, \omega\rangle$), ω denotes the pumping frequency, transmitted through the Au metasurface will be split into two parts: a residual RCP beam without a geometric phase and a left circularly polarized (LCP; $|-, \omega\rangle$) beam with a geometric phase $e^{i2\theta}$. In coherent SHG, two components will emerge according to the nonlinear conversion rules described above: a second-harmonic RCP beam ($|+, 2\omega\rangle$) from the K valley with double geometric phase $e^{i4\theta}$ and a second-harmonic LCP ($|-, 2\omega\rangle$) beam from the K' valley without any geometric phase. Thus, a spin-dependent phase gradient ($\nabla\phi$) could be imparted to the second-harmonic photons when θ changes spatially. This phase gradient provides the momentum matching to steer the valley second-harmonic photons in different directions according to the generalized Snell's law^{20,30,31}, $k_x \hat{x} = \nabla\phi$. More theoretical details are provided in Supplementary Section 4. Only the in-plane electric field ($E_x \hat{x} + iE_y \hat{y}$) can pump and interact with the valleys of 2D TMDCs effectively¹³. These in-plane components are also the ones that the Au metasurface can manipulate, because the Jones matrix operates on only the x and y components of the incident field.

Experimental demonstration

To verify our concept experimentally, arrays of rectangular nanoholes arranged in a hexagonal lattice were fabricated by using

focused ion beam milling (FEI Versa 3D). The thickness of the Au film is 60 nm , the unit-cell periodicity is 730 nm , and the length and width of the rectangular nanoholes are 335 nm and 145 nm , respectively. The rotation angle responsible for the phase gradient in our metasurface is governed by $\partial_x \theta = \pi/\Lambda$ (see Supplementary Fig. 4a). Here, $\Lambda = 4.2 \mu\text{m}$ is the spatial period of the full π rotation angle variation. Two-photon luminescence experiments were performed to determine the degenerate valley bandgap, which was found to be 2.004 eV (see Supplementary Fig. 2). To tune the polarization of the incident beam, a quarter-wave plate (QWP1) was inserted between the laser and the Au-WS₂ sample. The fundamental-frequency beam focused by a lens ($f = 8 \text{ cm}$) pumps the sample. The emitted signal was collected by an objective lens, filtered spectrally and imported to a spectrometer and a complementary metal oxide–semiconductor (CMOS) camera with an imaging tube lens. For the propagation measurement, we captured the SHG signals at propagation planes from $0 \mu\text{m}$ to $200 \mu\text{m}$ along the z axis in steps of $15 \mu\text{m}$. The polarization of the emitted SHG beam was extracted by a Glan-laser polarizer with a second quarter-wave plate (QWP2) at $z = 120 \mu\text{m}$. All optical measurements were performed at room temperature. More details of the sample fabrication and optical measurement are provided in the Methods.

Linearly polarized field pumping. We first test our synthetic metasurface with linearly polarized illumination (QWP1 is removed

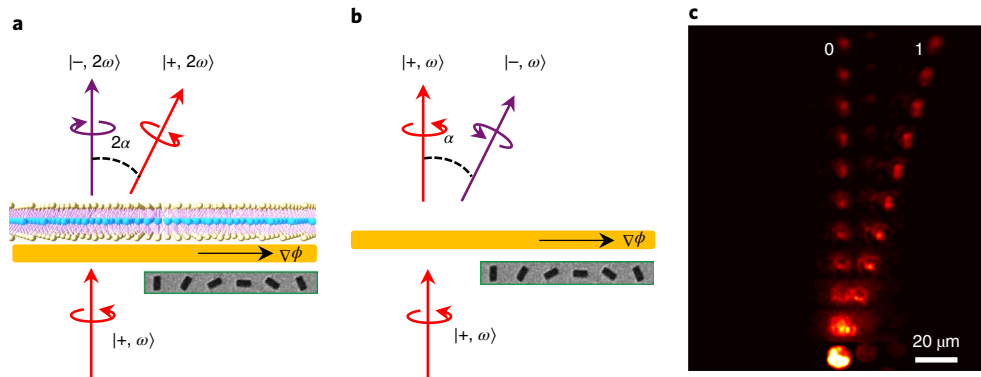


Fig. 3 | Schematic and experimental comparison for the synthetic Au-WS₂ metasurface under RCP pumping. **a, b**, Schematic representations of steering second-harmonic waves on RCP pumping with monolayer WS₂ (**a**) and of the photonic spin-Hall effect without WS₂ (**b**). In contrast to the photonic spin-Hall effect shown in **b**, the steered photon in **a** is the co-polarized component in the hybridized structure with the double steering angle. The inset SEM images show one period of the nanohole array in the range of Λ . **c**, Evolution of the light field for the case shown in **a**, as measured in the image plane at different propagation distances. '0' and '1' label the intensity order.

in this case). As the evolutionary light trajectory measured along the x - z plane illustrates (see Fig. 2e), SHG photons are split into three beams (-1 st, 0 th and $+1$ st order) in the image plane measured at the propagation length $z = 120 \mu\text{m}$ changes from being strongest (nearly vanishing) when the rotation angle ψ of the polarizer is 0° to nearly vanishing (strongest) at $\psi = 90^\circ$ and, finally, to being strongest again (nearly vanishing) when $\psi = 180^\circ$. By contrast, the 0 th-order intensity remains unchanged while ψ is varied. Such features are compatible with the picture described above with regards to the close relation that exists between the geometric phase added by the Au metasurface to impinging fundamental-frequency photons and the chirality of second-harmonic photons emitted from different valleys of 2D TMDCs. Within this scheme, second-harmonic photons with a geometric phase of $e^{i2\theta}$ (1 st order) would have a predominant RCP character and correspond to excitons created in K valleys, after two LCP photons are converted by the WS₂ layer following the scheme depicted in Fig. 1d: one incident RCP photon that has acquired a geometric phase $e^{i2\theta}$ and changed its chirality after passing through the Au metasurface, and an incident LCP photon being transmitted without any alteration after its passage through the same metasurface. In a complementary fashion, second-harmonic photons with a geometric phase of $e^{-i2\theta}$ (-1 st order) have a LCP character and are associated with excitons emerging from K' valleys. To corroborate this quantitatively, we also measured the intensity of the LCP and RCP components of those orders (see Fig. 2a–c). These results further support the claim that the designed Au metasurface can spatially separate second-harmonic photons from different valleys. To characterize the figure of merit of accessing the valleys via the Au metasurface in free space, we calculate the third Stokes parameter ($S_3 = (I_{\text{RCP}} - I_{\text{LCP}})/(I_{\text{RCP}} + I_{\text{LCP}})$) by measuring the averaged photon counts per unit area of the SHG spot. The measured S_3 of -1 st, 0 th and $+1$ st orders are -0.94 , -0.16 and 0.88 , respectively, indicating the nearly-perfect figure of merit of our designed Au-WS₂ metasurface. The minor deviation of S_3 from perfect circular polarization ($S_3 = \pm 1$) or linear polarization ($S_3 = 0$) could come from an undesired oblique propagation and the experimental tolerance in measurements. Thus, it can be concluded that the nonlinear chiral photons from different valleys are separated in free space.

Another quantitative characterization is the deflection angle α of the -1 st and 1 st orders. This angle is linked to the geometric phase introduced by the nanohole array and depends on the period of the phase gradient associated with the design of the Au metasurface as $k_{\text{SHG}} \sin \alpha = \pm 2\pi/\Lambda$ (where k_{SHG} denotes the free-space

wavevector of a SHG photon, see Supplementary Section 4). This equation predicts $\alpha = \pm 8.47^\circ$, which matches very well with the experimental value of $\pm 8.5^\circ$. Moreover, the intensity ratio of the $+1$ st, 0 th and -1 st orders is measured as $1.58:1:1.53$, which is remarkably consistent with the theoretical expectation of $1.59:1:1.59$ ($2|t_x^2 - t_y^2|^2 : |t_x + t_y|^2 : 2|t_x^2 - t_y^2|^2$). In principle, there would be two more diffraction orders (± 2 nd) of SHG under linearly polarized pumping, with deflection angles of around $\pm 17^\circ$, governed by $k_{\text{SHG}} \sin \alpha' = \pm 4\pi/\Lambda$. Their intensities should be around one-third that of the 0 th order (see Supplementary Section 4). These second-order beams also appear in our experiments (see Supplementary Fig. 4), but their measured intensities are much lower than the predicted ones, owing to the limited diffraction and collection efficiencies of our experimental apparatus.

Circularly polarized field pumping. We then switch the linearly polarized pumping to RCP illumination (see Fig. 3a). QWP1 is now placed between the laser and the synthetic metasurface. The measured second-harmonic intensity at different propagation lengths is shown in Fig. 3c. Only two orders are clearly observed: the 0 th order of cross-polarized light ($|-, 2\omega\rangle$) emitted from the K' valley and the 1 st order of co-polarized light ($|+, 2\omega\rangle$) from the K valley. The experimentally measured S_3 values are -0.99 and 0.94 , respectively. Conventional geometric-phase transmissive metasurfaces, linear (Fig. 3b) or nonlinear^{21,35,44,45}, always steer the light with opposite spin, owing to the spin-conversion process associated with the spin-orbit interaction. However, the exotic valley degree of freedom introduced by monolayer TMDCs displays a counter-spin SHG selection rule, allowing nonlinear photons with the same spins to be deflected (see Fig. 3a). This finding reveals the critical role of the valley index in the photonic spin-Hall process associated with our synthetic metasurface.

Another interesting feature is the spatial deflection angle of the 1 st order under RCP pumping (17.5°), which is approximately double of that of the 1 st order when the structure is illuminated by linearly polarized light (8.5°). In the case of RCP illumination, the two LCP photons needed to create an exciton in the K valley must have originated from two incident RCP photons that have both changed their chiralities and acquired a geometric phase $e^{i2\theta}$ after passing through the Au metasurface. Therefore, the geometric phase of the second-harmonic photons is $e^{i4\theta}$ in this case. On the other hand, second-harmonic photons emitted from K' valleys originate from the incident RCP photons that have been transmitted without spin conversion through the Au metasurface.

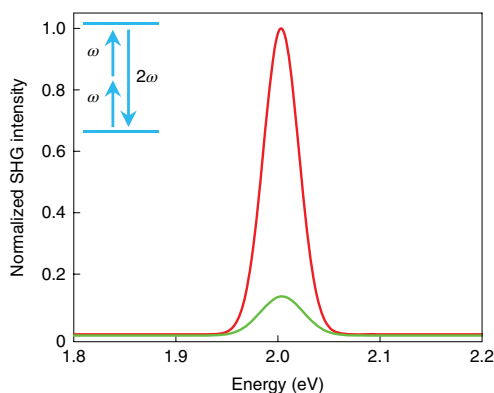


Fig. 4 | SHG enhancement in the synthetic Au-WS₂ metasurface. The SHG signal from a WS₂ monolayer on top of a Au metasurface (red line) and a quartz substrate (green line) with a circularly polarized fundamental-frequency beam is shown. The fundamental energy of the excitation signal is 1.002 eV. The inset shows the SHG process.

Metasurface-enabled plasmonic enhancement of SHG

The second-harmonic nonlinearity of pure WS₂ has been reported to be as large as 5 nm V⁻¹ (ref. 15), several orders of magnitude larger than in traditional nonlinear PhCs. However, the few-atom thickness of monolayer TMDCs limits the nonlinear light-matter interaction substantially. In Fig. 4 we compare the normalized SHG intensity of WS₂ on top of the plasmonic metasurface with that when the monolayer semiconductor is placed on a quartz substrate. We observe an enhancement of the SHG intensity by one order of magnitude in our synthetic metasurface. As shown in Supplementary Fig. 7, the SHG could be enhanced at the valley-exciton resonance^{6,12,13}, while our metasurface with large near-field enhancement could further boost SHG owing to the excitation of a plasmonic resonance^{46,47} at the fundamental frequency (Supplementary Fig. 3c,d). Finite-difference time-domain simulations (see Methods) reveal the emergence of a large plasmonic field localization at the metasurface–air interface, as depicted in Supplementary Fig. 3e,f. These simulations show that the main contributions to the SHG originating from the monolayer WS₂ were from regions near the nanoholes, as the plasmonic field is highly concentrated in these areas. The average fundamental-frequency field ($|E_x(\omega)|^2 + |E_y(\omega)|^2$) within the nanohole area is estimated to be enhanced by a factor of around 33. Taking the area ratio of the nanohole (about 0.1) into account, the average second-harmonic field intensity enhancement is estimated to be around tenfold ($(33 \times 0.1)^2$) according to the normalization method discussed by Wang et al.⁴⁶. This large value agrees well with the experimental result shown in Fig. 4, as well as the results of a rigorous nonlinear scattering theory (see Supplementary Section 6). Larger SHG intensity could be expected from topologically optimizing the properties of the nanostructure, such as the size of the nanoholes and the unit-cell periodicity of the array, but a tenfold enhancement is large enough to demonstrate the boosted light–matter interaction in our synthetic metasurface for nonlinear optical and optoelectronic applications¹⁶. Not limited to our Au metasurface, low-loss dielectric metasurfaces supporting Mie resonances could potentially be explored in the future to further boost the nonlinear response of 2D TMDCs^{48–50}.

Conclusion

In summary, we have proposed a synthetic metasurface that combines a plasmonic spin-Hall metasurface and a WS₂ monolayer. It provides a photonic pathway to manipulate the valley-locked nonlinear emission and creates a nonlinear chiral valley–photon interface at room temperature. An enhancement of the SHG by one

order of magnitude is achieved as a result of the high near-field confinement of light. This could be further enhanced by tuning the geometric parameters of the Au metasurface. In addition, the photonic spin–orbit coupling can induce a chirality-related geometric phase that interacts with the different valleys of monolayer WS₂ and steers the nonlinear valley–exciton-locked emission in any direction in free space, without requiring external stimuli such as an electric bias or magnetic field. Our strategy is of high fidelity and can be extended to other nanophotonic systems such as all-dielectric resonant metasurfaces and other TMDC monolayers. In future studies, the optical pumping or electron spin injection used to prepare the valley could be integrated into our synthetic metasurface to control the valley emission. Our work could provide a way to manipulate the valley–exciton transport, steer the spin–valley–exciton emission with nonlinear chiral valley–photon interfaces, and encode the valley index into free space.

Online content

Any methods, additional references, Nature Research reporting summaries, source data, statements of data availability and associated accession codes are available at <https://doi.org/10.1038/s41566-019-0399-1>.

Received: 19 October 2018; Accepted: 25 February 2019;

Published online: 1 April 2019

References

- Xiao, D., Yao, W. & Niu, Q. Valley-contrasting physics in graphene: magnetic moment and topological transport. *Phys. Rev. Lett.* **99**, 236809 (2007).
- Yao, W., Xiao, D. & Niu, Q. Valley-dependent optoelectronics from inversion symmetry breaking. *Phys. Rev. B* **77**, 235406 (2008).
- Ross, J. S. et al. Electrical control of neutral and charged excitons in a monolayer semiconductor. *Nat. Commun.* **4**, 1474 (2013).
- Mak, K. F., He, K., Shan, J. & Heinz, T. F. Control of valley polarization in monolayer MoS₂ by optical helicity. *Nat. Nanotechnol.* **7**, 494–498 (2012).
- Zeng, H., Dai, J., Yao, W., Xiao, D. & Cui, X. Valley polarization in MoS₂ monolayers by optical pumping. *Nat. Nanotechnol.* **7**, 490–493 (2012).
- Xiao, J. et al. Nonlinear optical selection rule based on valley-exciton locking in monolayer WS₂. *Light Sci. Appl.* **4**, e366 (2015).
- Sun, Z. et al. Optical control of room-temperature valley polaritons. *Nat. Photon.* **11**, 491–496 (2017).
- Mak, K. F., Lee, C., Hone, J., Shan, J. & Heinz, T. F. Atomically thin MoS₂: a new direct-gap semiconductor. *Phys. Rev. Lett.* **105**, 136805 (2010).
- Novoselov, K. S. et al. Two-dimensional atomic crystals. *Proc. Natl Acad. Sci. USA* **102**, 10451–10453 (2005).
- Splendiani, A. et al. Emerging photoluminescence in monolayer MoS₂. *Nano Lett.* **10**, 1271–1275 (2010).
- Novoselov, K. S., Mishchenko, A., Carvalho, A. & Castro Neto, A. H. 2D materials and van der Waals heterostructures. *Science* **353**, aac9439 (2016).
- Seyler, K. L. et al. Electrical control of second-harmonic generation in a WSe₂ monolayer transistor. *Nat. Nanotechnol.* **10**, 407–411 (2015).
- Wang, G. et al. Giant enhancement of the optical second-harmonic emission of WSe₂ monolayers by laser excitation at exciton resonances. *Phys. Rev. Lett.* **114**, 097403 (2015).
- Selig, M. et al. Excitonic linewidth and coherence lifetime in monolayer transition metal dichalcogenides. *Nat. Commun.* **7**, 13279 (2016).
- Janisch, C. et al. Extraordinary second harmonic generation in tungsten disulfide monolayers. *Sci. Rep.* **4**, 5530 (2014).
- Zhao, M. et al. Atomically phase-matched second-harmonic generation in a 2D crystal. *Light Sci. Appl.* **5**, e16131 (2016).
- Yu, H., Cui, X., Xu, X. & Yao, W. Valley excitons in two-dimensional semiconductors. *Natl Sci. Rev.* **2**, 57–70 (2015).
- Mak, K. F. & Shan, J. Photonics and optoelectronics of 2D semiconductor transition metal dichalcogenides. *Nat. Photon.* **10**, 216–226 (2016).
- Mak, K. F., Xiao, D. & Shan, J. Light–valley interactions in 2D semiconductors. *Nat. Photon.* **12**, 451–460 (2018).
- Yu, N. et al. Light propagation with phase discontinuities: generalized laws of reflection and refraction. *Science* **334**, 333–337 (2011).
- Meinzer, N., Barnes, W. L. & Hooper, I. R. Plasmonic meta-atoms and metasurfaces. *Nat. Photon.* **8**, 889–898 (2014).
- Khorasaninejad, M. et al. Metalenses at visible wavelengths: diffraction-limited focusing and subwavelength resolution imaging. *Science* **352**, 1190–1194 (2016).

23. Chen, X. et al. Dual-polarity plasmonic metalens for visible light. *Nat. Commun.* **3**, 1198 (2012).
24. Zheng, G. et al. Metasurface holograms reaching 80% efficiency. *Nat. Nanotechnol.* **10**, 308–312 (2015).
25. Ni, X., Wong, Z. J., Mrejen, M., Wang, Y. & Zhang, X. An ultrathin invisibility skin cloak for visible light. *Science* **349**, 1310–1314 (2015).
26. Lin, D., Fan, P., Hasman, E. & Brongersma, M. L. Dielectric gradient metasurface optical elements. *Science* **345**, 298–302 (2014).
27. Shitrit, N. et al. Spin-optical metamaterial route to spin-controlled photonics. *Science* **340**, 724–726 (2013).
28. Tittl, A. et al. Imaging-based molecular barcoding with pixelated dielectric metasurfaces. *Science* **360**, 1105–1109 (2018).
29. Arbabi, A., Horie, Y., Bagheri, M. & Faraon, A. Dielectric metasurfaces for complete control of phase and polarization with subwavelength spatial resolution and high transmission. *Nat. Nanotechnol.* **10**, 937–943 (2015).
30. Yin, X., Ye, Z., Rho, J., Wang, Y. & Zhang, X. Photonic spin Hall effect at metasurfaces. *Science* **339**, 1405–1407 (2013).
31. Ling, X. et al. Giant photonic spin Hall effect in momentum space in a structured metamaterial with spatially varying birefringence. *Light Sci. Appl.* **4**, e290 (2015).
32. Zhou, J. et al. Broadband photonic spin Hall meta-Lens. *ACS Nano* **12**, 82–88 (2018).
33. Lin, J. et al. Polarization-controlled tunable directional coupling of surface plasmon polaritons. *Science* **340**, 331–334 (2013).
34. High, A. A. et al. Visible-frequency hyperbolic metasurface. *Nature* **522**, 192–196 (2015).
35. Ling, X. et al. Recent advances in the spin Hall effect of light. *Rep. Prog. Phys.* **80**, 066401 (2017).
36. Sattari, H., Rashed, A. R., Ozbay, E. & Caglayan, H. Bright off-axis directional emission with plasmonic corrugations. *Opt. Express* **25**, 30827–30842 (2017).
37. Li, D. et al. Unidirectional surface plasmon-polariton excitation by a compact slot partially filled with dielectric. *Opt. Express* **21**, 5949–5956 (2013).
38. Sun, L. et al. Routing valley excitons in a monolayer MoS₂ with a metasurface. Preprint at <https://arxiv.org/abs/1801.06543> (2018).
39. Chervy, T. et al. Room temperature chiral coupling of valley excitons with spin-momentum locked surface plasmons. *ACS Photon.* **5**, 1281–1287 (2018).
40. Bliokh, K. Y., Rodriguez-Fortuño, F. J., Nori, F. & Zayats, A. V. Spin-orbit interactions of light. *Nat. Photon.* **9**, 796–808 (2015).
41. Tan, Q., Guo, Q., Liu, H., Huang, X. & Zhang, S. Controlling the plasmonic orbital angular momentum by combining the geometric and dynamic phases. *Nanoscale* **9**, 4944–4949 (2017).
42. Bomzon, Z., Biener, G., Kleiner, V. & Hasman, E. Space-variant Pancharatnam–Berry phase optical elements with computer-generated subwavelength gratings. *Opt. Lett.* **27**, 1141–1143 (2002).
43. Jones, A. M. et al. Optical generation of excitonic valley coherence in monolayer WSe₂. *Nat. Nanotechnol.* **8**, 634–638 (2013).
44. Li, G. et al. Continuous control of the nonlinearity phase for harmonic generations. *Nat. Mater.* **14**, 607–612 (2015).
45. Tymchenko, M. et al. Gradient nonlinear Pancharatnam–Berry metasurfaces. *Phys. Rev. Lett.* **115**, 207403 (2015).
46. Wang, Z. et al. Selectively plasmon-enhanced second-harmonic generation from monolayer tungsten diselenide on flexible substrates. *ACS Nano* **12**, 1859–1867 (2018).
47. Chen, J. et al. Tungsten disulfide–gold nanohole hybrid metasurfaces for nonlinear metalenses in the visible region. *Nano Lett.* **18**, 1344–1350 (2018).
48. Chen, H. et al. Enhanced second-harmonic generation from two-dimensional MoSe₂ on a silicon waveguide. *Light Sci. Appl.* **6**, e17060 (2017).
49. Kuznetsov, A. I., Miroshnichenko, A. E., Brongersma, M. L., Kivshar, Y. S. & Luk'yanchuk, B. Optically resonant dielectric nanostructures. *Science* **354**, aag2472 (2016).
50. Cihan, A. F., Curto, A. G., Raza, S., Kik, P. G. & Brongersma, M. L. Silicon Mie resonators for highly directional light emission from monolayer MoS₂. *Nat. Photon.* **12**, 284–290 (2018).

Acknowledgements

The work done at Huazhong University of Science and Technology was supported by the National Natural Science Foundation of China (grant numbers 91850113, 11774115 and 11674117) and the 973 Programs under grant number 2014CB921301. We thank the Center of Nano-Science and Technology of Wuhan University for their support in sample fabrication. J.W. acknowledges financial support from the A*Star – Science and Engineering Research Council Pharos Program (grant number 15270 00015). S.Z. acknowledges support from ERC Consolidator Award (TOPOLOGICAL). F.G.-V. acknowledges financial support from the Spanish MINECO under contract no. MAT2014-53432-C5-5-R and the “María de Maeztu” programme for Units of Excellence in R&D (MDM-2014-0377). C.-W.Q. acknowledges financial support from A*STAR Pharos Program (grant number 15270 00014, with project number R-263-000-B91-305) and the National Research Foundation, Prime Minister’s Office, Singapore, under its Competitive Research Program (CRP award number NRF-CRP 15-2015-03).

Author contributions

K.W., P.L., C.-W.Q. and G.H. conceived the idea. K.W., P.L. and C.-W.Q. supervised the project. G.H., K.W. and C.-W.Q. designed the experiments. X.H., K.W., W.Z., W.L. and B.W. performed the experiments. G.H., J.W., K.W., H.-X.X., S.Z., F.G.-V., P.L. and C.-W.Q. analysed the data. G.H., F.G.-V. and C.-W.Q. drafted the paper with input from all authors.

Competing interests

The authors declare no competing interests.

Additional information

Supplementary information is available for this paper at <https://doi.org/10.1038/s41566-019-0399-1>.

Reprints and permissions information is available at www.nature.com/reprints.

Correspondence and requests for materials should be addressed to K.W., P.L. or C.-W.Q.

Publisher’s note: Springer Nature remains neutral with regard to jurisdictional claims in published maps and institutional affiliations.

© The Author(s), under exclusive licence to Springer Nature Limited 2019

Methods

Sample fabrication. *Lift-off process for the WS₂ monolayer.* First, 1 g of polymethyl methacrylate (PMMA; Aldrich; average molecular weight, 996,000) was dissolved in anisole to prepare 50 g of solution (2 wt%). A few drops of this solution were drop-coated on the sapphire substrate with WS₂ monolayer flakes until it fully covered the substrate. The coated substrate was then placed at room temperature for more than 1.5 h to allow the anisole to evaporate, followed by a curing step of baking at 120 °C for 0.5 h. Polymer strips (1 mm in width) were scratched by a blade at the edges of the substrate to reduce the lift-off time. The substrate was immersed in 3 mol l⁻¹ NaOH aqueous solution at room temperature for more than 4 h to etch the sapphire surface, and the PMMA–WS₂ films lifted off from the growth substrate naturally. The films were fished out with a glass slide and immersed in deionized water three times to remove the residual NaOH solution.

Fabrication of Au metasurfaces. A 60-nm-thick Au film with a 5-nm-thick Cr adhesion layer was deposited on a quartz substrate by using an e-beam evaporator. The rectangular nanohole array was milled on the film using focused ion beam milling (FEI Versa 3D).

Transfer process for the WS₂ monolayers. The PMMA–WS₂ films were fished out with the fabricated metasurfaces with tweezers. These were then quickly aligned with the metasurface arrays under a microscope before the water dried. The substrate was then baked at 120 °C for 1 h to improve the adhesion between the WS₂ monolayers and the Au metasurfaces. Finally, the substrate was immersed in acetone three times (each time for 15 mins) to remove the PMMA film.

Optical measurement. A mode-locked Ti:sapphire femtosecond laser system (Astrella Coherent; 35 fs, 800 nm, 1 kHz) and an optical parametric amplifier (TOPAS-Prime Plus, Light Conversion) were used as the fundamental beam at

1,240 nm with linear polarization. The polarization of the fundamental beam can be further adjusted by QWP1 (WPQW-IR-4M, Sigma Koki; 1,000–1,600 nm) to generate circular polarization. The beam was then focused by an 8 cm lens to pump the sample for SHG. An objective (Olympus; ×40, 0.65 NA) was used to collect the emissions from the sample. After being filtered out of the fundamental beam, the emitted signals were imported directly to a spectrometer (Shamrock 303i, Andor) or a CMOS camera (Prime 95B, PHOTOMETRICS) with a tube lens for imaging. By moving the objective along the *z* axis, the images of the emitted signals were captured at different planes along the *z* axis in steps of 15 μm. The polarization of the emitted second-harmonic signal was extracted by a Glan-laser polarizer (GL10P-A, Thorlabs; 400–700 nm) with QWP2 at the second-harmonic wavelength (WPQ05M-633, Thorlabs). The axis of the Glan-laser polarizer was set to be vertical (horizontal) to extract the RCP (LCP) component, by rotating the fast axis of QWP2 by 45° (–45°). The Stokes parameters were determined by rotating the quarter-wave plate from 0° to 180° in steps of 10°.

Numerical simulation. The finite-difference time-domain simulation was performed using the commercially available software Lumerical 2017b (<http://www.lumerical.com/tcad-products/fdtd/>). The local field enhancement factor at the metasurface–air interface was obtained by taking the average of the electric field in the plane. The transmission coefficients along the *x* and *y* directions were obtained by probing the field of the far-field monitor. The simulation results for the transmission coefficients along the two principal directions at the incident fundamental-frequency light are $t_x = 0.0961e^{2.1763i}$ and $t_y = 0.7183e^{-2.9896i}$. More details are provided in the Supplementary Information.

Data availability

The data that support the plots within this paper and other findings of this study are available from the corresponding authors upon reasonable request.